



A facile approach to tailor electrocatalytic properties of MnO₂ through tuning phase transition, surface morphology and band structure

Yingze Zhou^a, Zizhen Zhou^a, Long Hu^a, Ruoming Tian^b, Yuan Wang^c, Hamid Arandiyani^{c,d}, Fandi Chen^a, Mengyao Li^{a,*}, Tao Wan^{a,*}, Zhaojun Han^e, Zhipeng Ma^e, Xunyu Lu^e, Claudio Cazorla^{f,*}, Tom Wu^a, Dewei Chu^a

^a School of Materials Science and Engineering, The University of New South Wales, Sydney 2052, Australia

^b Mark Wainwright Analytical Centre, University of New South Wales, Sydney, NSW 2052, Australia

^c School of Science, RMIT University, Melbourne, Victoria 3001, Australia

^d Laboratory of Advanced Catalysis for Sustainability, School of Chemistry, University of Sydney, Sydney, NSW 2006, Australia

^e School of Chemical Engineering, The University of New South Wales, Sydney 2052, Australia

^f Departament de Física, Universitat Politècnica de Catalunya, Campus Nord B4-B5, E-08034 Barcelona, Spain

ARTICLE INFO

Keywords:

MnO₂ phase transition
One-step hydrothermal method
Nanowire-nanosheet
Electrocatalyst
Band structure
Density functional theory

ABSTRACT

The structural and electronic properties of MnO₂ based electrocatalysts are key factors determining their electrochemical performance. To date, it is still challenging to synergistically tune the crystal structure, morphology, and electronic band (i.e., band gap and band alignments) of MnO₂ through facile synthesis approaches. This study has reported a one-step hydrothermal method to synthesize a prototypical MnO₂ electrocatalyst with optimized structural and electrochemical properties. By simply adjusting the hydrothermal time, the phase transition from polymorphic δ to α can be induced in MnO₂. The obtained nanowires on nanosheets structure grown in-situ on nickel foam provides a large surface area, great accessible active sites, and good mass/charge transfer efficiency. Further investigation through first-principles calculations reveals that compared to δ -MnO₂, the α -MnO₂ polymorph with rich oxygen vacancies has better band-alignment tunability, which is also beneficial for improving the electrochemical performance. The α phase MnO₂ exhibits superior catalytic performance for both OER and HER (OER overpotential of 0.45 V at 50 mA cm⁻² and HER overpotential of 0.14 V at 50 mA cm⁻²). The developed synthesis method can be extended to catalyst designs that require precise control of phase and morphology evolution in a wide range of applications.

1. Introduction

Electrochemical water splitting is considered to be one of the most promising green hydrogen production methods [1,2]. To date, remarkable progress in high efficient noble metal-based electro-catalysts, such as Pt [3], Ru [4], and Ir [5] has been achieved through materials engineering [6,7]. However, there are still some unsolved issues in the current research, such as the high cost and limited earth reserves of precious metal catalysts, which greatly restrict their wide applications for water splitting. Recently, non-precious metal-based electrocatalysts are attracting increasing attention for practical water splitting applications [8–14]. Among them, MnO₂ is a promising candidate owing to its high natural abundance, low cost, and environmental friendliness [15–18].

To enable superior performance of MnO₂ as a catalyst, the materials design is vital yet challenging because the catalytic activity is strongly affected by multiple correlated factors: (1) the crystalline structure; it has been evidenced that polymorph α -MnO₂ (alpha phase) shows higher catalytic activity in oxygen evolution reaction (OER) than β -MnO₂ (beta phase) and δ -MnO₂ (delta phase) owing to its lower charge-transfer resistance and enhanced O₂ adsorption capability; [19] (2) the surface morphology; numerous works have shown that 1-D dimensional nanostructures containing a large number of exposed active sites exhibit better electrocatalytic activities; [20] (3) The defect engineering; the amount of Mn³⁺ and oxygen vacancies (Vo) are believed to be beneficial for the catalytic performance; [16,21] and (4) the electronic band structure; the well-matched band-alignment could accelerate the charge injection rate in electrocatalytic reactions, [22,23] thus improving

* Corresponding authors.

E-mail addresses: mengyao.li1@unsw.edu.au (M. Li), tao.wan@unsw.edu.au (T. Wan), claudio.cazorla@upc.edu (C. Cazorla).

<https://doi.org/10.1016/j.cej.2022.135561>

Received 12 November 2021; Received in revised form 12 February 2022; Accepted 26 February 2022

Available online 1 March 2022

1385-8947/© 2022 Elsevier B.V. All rights reserved.

catalytic performance. Many strategies have been adapted to optimize the aforementioned parameters through tuning reaction precursors and engineering doping additives [24]. However, facile and effective methods to synthesize MnO_2 with the combined merits such as desired crystalline structure, optimized surface morphology, suitable $\text{Mn}^{3+}/\text{Mn}^{4+}$ ratio, and matched band structure properties (e.g., reduced energy band gap) are still not available at the moment.

Herein, we design a facile one-step hydrothermal approach using KMnO_4 aqueous solution as an exclusive precursor to prepare nanostructured MnO_2 with desirably combined merits for efficient electrocatalysis applications. Through simply tuning the reaction time, controllable phase transformation and superior surface morphology of MnO_2 was successfully realized. The resulting MnO_2 was then applied as the electrodes for investigating water splitting performance. It was found that both the OER and hydrogen evolution reaction (HER) performances have been improved in $\alpha\text{-MnO}_2$ electrocatalyst owing to the improved charge transfer efficiency and effective surface area. First-principles calculations reveal that the resulting $\alpha\text{-MnO}_2$ has an appropriate energy band gap and band-alignment tunability for water-splitting applications, thus enabling enhanced electrocatalytic performance. Based on our experimental and theoretical results, this work provides a guideline to prepare MnO_2 with desirable properties for the development of highly active, cost-effective, and stable catalysts for electrochemical water splitting applications.

2. Experimental section

2.1. Preparation of MnO_2 nanostructures on nickel foam (NF)

All chemicals were purchased from Sigma-Aldrich and used directly. The MnO_2 -NF samples were synthesized using a facile hydrothermal method. In this work, the NF (2.5×3 cm) was cleaned with hydrochloric acid (3.0 M) for 15 min to remove the nickel oxides, followed by rinsing with Milli-Q water and ethanol three times. The solution was prepared by dissolving 0.15 M KMnO_4 in 30 mL of deionized water under mechanical stirring and then transferred to a 50-mL Teflon-lined autoclave containing cleaned NF. The autoclave was heated at 220 °C for various reaction times (MnO_2 -NF-xh). After cooling to room temperature naturally, the MnO_2 -NF products were washed with Milli-Q water and ethanol three times, followed by drying in air at 80 °C for 12 h. (The 3 h reaction time was reported in our previous work [25])

2.2. Material characterization

The crystal structures of MnO_2 were determined by X-ray diffraction (XRD, Empyrean II). Raman spectra were recorded using Renishaw inVia Raman Microscope (calibrated with Si single crystal). Scanning electron microscopy (SEM, Nova NanoSEM 450), transmission electron microscopy (TEM, JEOL JEM-F200), and energy dispersive spectroscopy (EDS) were employed to study morphology and elemental compositions. The elemental states and composition were obtained by X-ray photoelectron spectroscopy (XPS, Thermo ESCALAB250i). The C 1 s peak was calibrated binding energies at 284.8 eV. The electron paramagnetic resonance spectroscopy (EPR) was collected using Bruker EMX X-Band ESR Spectrometer. EPR spectra were obtained under 120 K. The sample amount used for EPR measurement was 15.0 mg.

2.3. Electrochemical measurement

The electrochemical measurements were carried out using a three-electrode cell on an Autolab PGSTAT302N electrochemical workstation and a CHI 760 electrochemical workstation. The synthesized MnO_2 -NF-xh samples were used as working electrodes directly. Ag/AgCl (3.5 M KCl) and graphite rods were applied as reference and counter electrodes, respectively. 1.0 M potassium hydroxide (KOH) was used as the electrolyte in this three-electrode system. All recorded potentials values

were then calibrated versus reversible hydrogen electrode (RHE) through the following Nernst equation:

$$E_{\text{RHE}} = E_{\text{Ag/AgCl}} + 0.2046 \text{ V} + 0.0592 \times \text{pH} \quad (1)$$

where E_{RHE} is the converted potential, and $E_{\text{Ag/AgCl}}$ is the experiment record. The working electrodes were scanned from 0 V to 0.8 V (vs. Ag/AgCl) at 50 mV s^{-1} to stabilization before testing. The linear sweep voltammetry (LSV) curves were employed to determine the OER and HER activities under 5 mV s^{-1} with 90% iR compensation. LSV curves were performed from 0 V to 0.8 V (vs. Ag/AgCl) for OER testing and -0.7 V to -1.5 V for HER testing. The stability measurement was determined at the overpotential point of 10 mA cm^{-2} and 100 mA cm^{-2} for 43,200 s (12 h). The electrochemical impedance spectroscopy (EIS) test was performed in the frequency range of 0.01 Hz to 100 kHz with an amplitude of 5 mV at a potential of 1.65 V vs RHE.

The electrochemical active surface area (ECSA) was converted from the electrochemical double-layer capacitance (C_{dl}) by performing cyclic voltammetry (CV) test. Five scan rates (5, 10, 20, 30, and 40 mV s^{-1}) were applied to the CV in the range of non-faradaic processes. C_{dl} was the slope of the linear fits of the capacitive current density at the average potential of each scan rate.

2.4. First-principles calculations

Spin-polarized density functional theory (DFT) [26] calculations were performed to theoretically characterise the electronic band structure properties (i.e., band gap and band alignments) of the α and δ polymorphs MnO_2 for both stoichiometric and non-stoichiometric compositions. The PBEsol + U exchange–correlation energy functional [27] was used as it is implemented in the VASP software [28]. A “Hubbard- U ” scheme [29] with $U = 3$ eV was employed for better treatment of the localized Mn 3d electronic orbitals. We employed the “projector augmented wave” method [30] to represent the ionic cores by considering the following electrons as valence: Mn 3d and 4s and O 2s and 2p. Wave functions were described in a plane-wave basis truncated at 650 eV. For integrations within the first Brillouin zone, we employed Monkhorst-Pack k-point grids with a density equivalent to that of a $10 \times 10 \times 16$ mesh for the bulk $\alpha\text{-MnO}_2$ unit cell. Periodic boundary conditions were applied along the three lattice vectors defining the simulation supercell. Geometry relaxations were performed with a conjugate-gradient algorithm that optimized the ionic positions and volume and shape of the simulation cell. The relaxations were halted when the forces in the atoms were all below $0.01 \text{ eV} \cdot \text{\AA}^{-1}$. By using these technical parameters, total energies were converged to within 0.5 meV per formula unit. Non-stoichiometric MnO_{2-x} systems were generated by removing one oxygen atom out of eight formula units (i.e., $\text{MnO}_{1.875}$). The range-separated hybrid HSE06 exchange–correlation functional [31] was used to accurately estimate the electronic properties of the equilibrium geometries determined at the PBEsol + U level.

The theoretical value of the valence and conduction energy band edges as referred to the vacuum level were determined through the standard DFT approach described in work [32]. In a nutshell, both bulk and slab calculations were performed to obtain the alignment of the electrostatic potential within the analyzed oxides by taking the vacuum level as reference. From the slab calculations, we obtained the macroscopic-average electrostatic potential within the semiconductors as referred to vacuum. The planar potential was computed by averaging potential values estimated within atomic planes oriented perpendicular to the slab surface, while the macroscopic-average electrostatic potential was obtained by taking averages of the planar potential over distances of one unit cell along the same direction. For these calculations, simulation cells containing ~ 2.0 nm thick oxide slabs and 2.5 nm thick vacuum regions were employed. We checked that the electron density in the center of the slabs was practically identical to those in the corresponding bulk materials.

3. Results and discussion

3.1. Phase transition of $\text{MnO}_2\text{-NF}$

Tuning the crystal structure of MnO_2 is critical towards enhanced electrochemical performance [19]. Herein, MnO_2 nanostructured materials with various crystal structures were synthesized by controlling the hydrothermal reaction time, in which the dark colour MnO_2 grew on nickel foam directly (Fig. S1). In the beginning, $\delta\text{-MnO}_2$ with a layered structure was grown on nickel foam substrates. Then the layered $\delta\text{-MnO}_2$ was transformed into the poor crystallinity intermediate state as the reaction continues. Subsequently, with further increasing reaction time, the MnO_2 was finally converted into well-crystallized $\alpha\text{-MnO}_2$.

To verify the evolution of the crystal structure of MnO_2 , X-ray diffraction (XRD) technique was used to characterize the crystal structures. To better understand the phase transformation process, five samples with reaction time at 3, 12, 24, 36, and 48 h were selected, which are named $\text{MnO}_2\text{-NF-3h}$, $\text{MnO}_2\text{-NF-12h}$, $\text{MnO}_2\text{-NF-24h}$, $\text{MnO}_2\text{-NF-36h}$, and $\text{MnO}_2\text{-NF-48h}$, respectively. As shown in Fig. 1a and S2, the $\text{MnO}_2\text{-NF-3h}$ is δ phase with layered structure ($\text{K}_{0.27}(\text{MnO}_2)\cdot(\text{H}_2\text{O})_{0.54}$, JCPDS 00-052-0556), where K^+ and H_2O were inserted into the interlayers of MnO_2 . Then the intermediate $\text{MnO}_2\text{-NF-12h}$ remains crystallized structures. However, as shown in Fig. S2c and d, the samples $\text{MnO}_2\text{-NF-24h}$ and $\text{MnO}_2\text{-NF-36h}$ exhibit weaker or unobservable peaks, which are generally considered as the intermediate state with poor crystallinity. Finally, the $\text{MnO}_2\text{-NF-48h}$ belongs to the pure phase of $\alpha\text{-MnO}_2$ (Fig. S2b, JCPDS 04-005-4884). With time increasing, MnO_2 transformed from δ structure to a poor crystallinity structure, followed by a transition to well-crystallized α structure. Additionally, no oxidized NF was observed for any samples under the detection limit. The XRD results prove our proposed processes of crystalline structure transform. Furthermore, the Raman spectra of the MnO_2 (Fig. 1b) show that $\text{MnO}_2\text{-NF-48h}$ (α phase) exhibits a prominent low-wavenumber peak at $\sim 181\text{ cm}^{-1}$, which can be assigned to an external mode that is derived from the translational motion of $[\text{MnO}_6]$ units [33]. The sharp peaks of $\text{MnO}_2\text{-NF-3h}$ and $\text{MnO}_2\text{-NF-48h}$ at ~ 580 and $\sim 640\text{ cm}^{-1}$ are caused by the stretching vibrations of Mn-O and Mn-O-Mn , respectively [34]. The results further confirm the successful synthesis of $\alpha\text{-MnO}_2$ and provide a guideline to accurately tune the crystal structure of MnO_2 for target-orientation applications by simply controlling the reaction time.

The surface morphology of MnO_2 plays a significant role in electrochemical performance, which is closely correlated with the number of exposed active sites [18,19]. As shown in Fig. 2a, MnO_2 nanosheets were vertically grown on the NF for 3 h, which is in good accordance with

reported results [16]. After a reaction of 48 h, a nanowire structure was found (Fig. 2b). The transmission electron microscopy (TEM) images inserted in Fig. 2c and d further confirm the formation of ultrathin nanosheets and ultra-long nanowires, respectively. In addition, the α phase MnO_2 nanopowders were synthesized as the control sample to observe the typical morphology of $\alpha\text{-MnO}_2$. As shown in Fig. S3, the $\alpha\text{-MnO}_2$ with 2×2 tunnel structures usually grows along the $[001]$ tunnel direction, which exhibits a nanowires/nanorods-like morphology [35]. Similarly, the nanowire morphologies appear under the long reaction time ($\text{MnO}_2\text{-NF-48h}$), evidencing that the phase transition happened with the prolonged hydrothermal treatment.

Furthermore, the high-resolution TEM (HR-TEM) images were used to examine the crystal lattice structure of different phases (Fig. 2c for the sample $\text{MnO}_2\text{-NF-3h}$ and Fig. 2d for the sample $\text{MnO}_2\text{-NF-48h}$). The clear lattice fringes with d-spacings of 0.714, 0.352, and 0.214 nm correspond to the (003), (006), and (015) diffraction planes of the $\delta\text{-MnO}_2$, respectively (JCPDS 00-052-0556); and the d-spacings of 0.695 and 0.238 nm correspond to the (110) and (121) diffraction planes of the $\alpha\text{-MnO}_2$, respectively (JCPDS 04-005-4884). These results are in good agreement with our XRD results. In addition, TEM-EDS mapping images indicate the uniform distribution of Mn, O, and K elements in nanostructured materials (Fig. 2e-h and 2i-l).

It is well known that the ratio of $\text{Mn}^{3+}/\text{Mn}^{4+}$ has an influence on electrocatalytic performance [9,16]. XPS measurements were performed to determine the evolution of manganese oxidation states. The XPS survey spectra for $\text{MnO}_2\text{-NF}$ (3 h and 48 h) show the presence of Mn, O, K, and C (Fig. S4). The elements identified by XPS are in good accordance with those in the EDS results (Fig. S5). Mn 2p XPS spectra (Fig. 3a and b) confirm the coexistence of Mn (III, Mn 2p_{3/2} peak centered at 642.0 eV) and Mn (IV, Mn 2p_{3/2} peak centered at 643.2 eV) in $\text{MnO}_2\text{-NF}$. The XPS spectra were recorded for the Mn 3s region (Fig. 3c and d). The multiple splitting (ΔE), which relates to the oxidation state, was 4.6 eV for the $\text{MnO}_2\text{-NF-3h}$ sample and 4.9 eV for the $\text{MnO}_2\text{-NF-48h}$ sample, indicating the average oxidation states (AOS) of 3.78 and 3.44 respectively ($\text{AOS} = 8.956 - 1.126 \times \Delta E$) [36]. The results indicate a further reduction of partial Mn^{4+} to Mn^{3+} . As shown in Fig. 3a and b, the ratio of $\text{Mn}^{3+}/\text{Mn}^{4+}$ in $\text{MnO}_2\text{-NF-48h}$ is $\approx 1.06:1$, which is much higher than that (0.36:1) in $\text{MnO}_2\text{-NF-3h}$. In addition, the V_o in $\text{MnO}_2\text{-NF}$ samples is associated with the proportion of Mn^{3+} centres as well [16]. The O 1s peak in XPS can be split into multiple peaks: the O_L peak at 530.1 eV ($\text{MnO}_2\text{-NF-3h}$) / 529.6 eV ($\text{MnO}_2\text{-NF-48h}$) are assigned to Mn-O-Mn bond (the 0.5 eV shift of different phases is in good accordance with previous reports [37,38]); the O_V peak at 531.1 eV belongs to oxygen-deficient regions within the lattice (Mn-O-H), and the O_C peak at

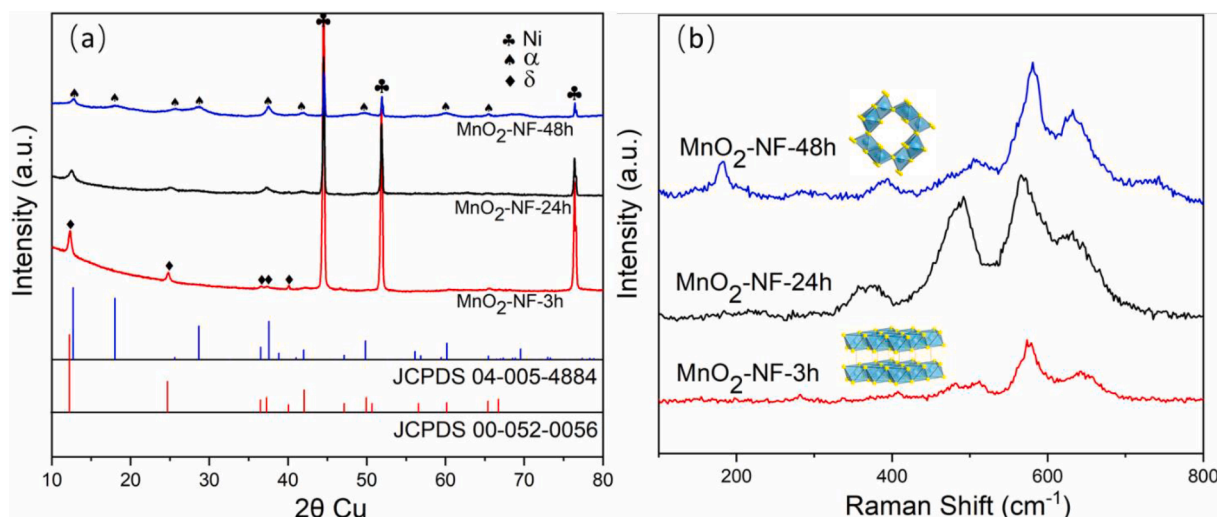


Fig. 1. (a) XRD patterns of $\text{MnO}_2\text{-NF-3h}$, $\text{MnO}_2\text{-NF-24h}$ and $\text{MnO}_2\text{-NF-48h}$; (b) Raman spectra of the $\text{MnO}_2\text{-NF-3h}$, $\text{MnO}_2\text{-NF-24h}$ and $\text{MnO}_2\text{-NF-48h}$.

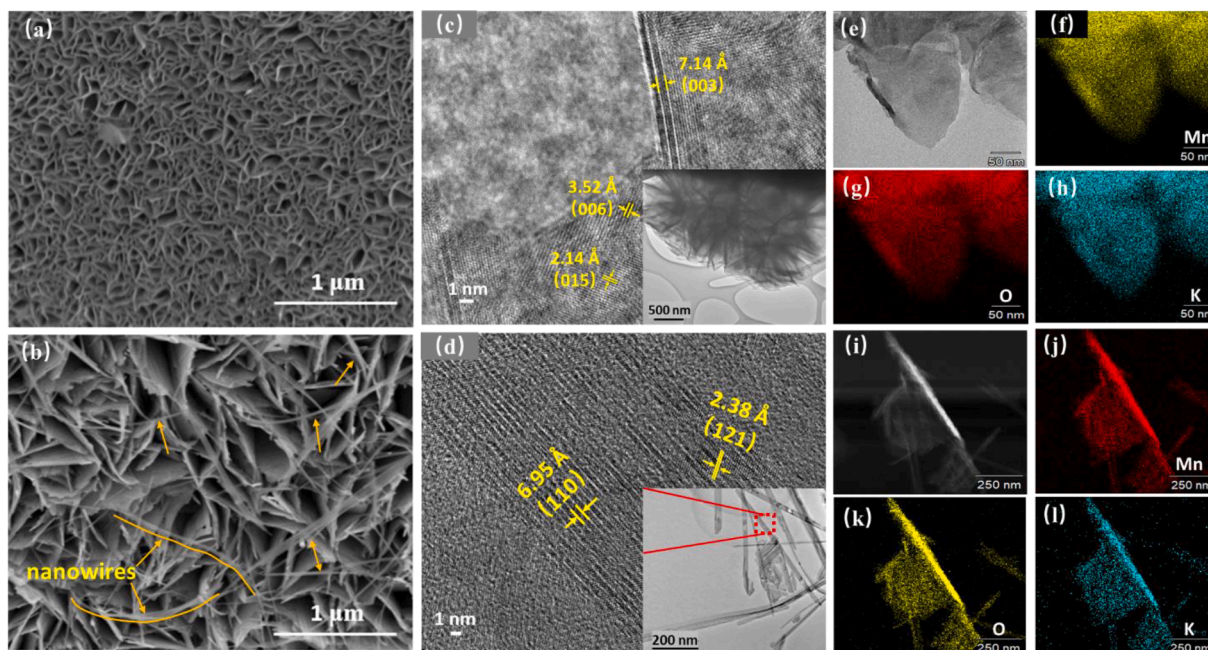


Fig. 2. SEM images of MnO₂-NF with different reaction times: (a) 3 h; (b) 48 h; (c) HR-TEM of MnO₂-NF-3h (the insert images are TEM of MnO₂-NF for 3 h); (d) HR-TEM of MnO₂-NF-48h (the insert images are TEM of MnO₂-NF for 48 h); (e)-(h) TEM-EDS of MnO₂-NF-3h; (i)-(l) TEM-EDS of MnO₂-NF-48h.

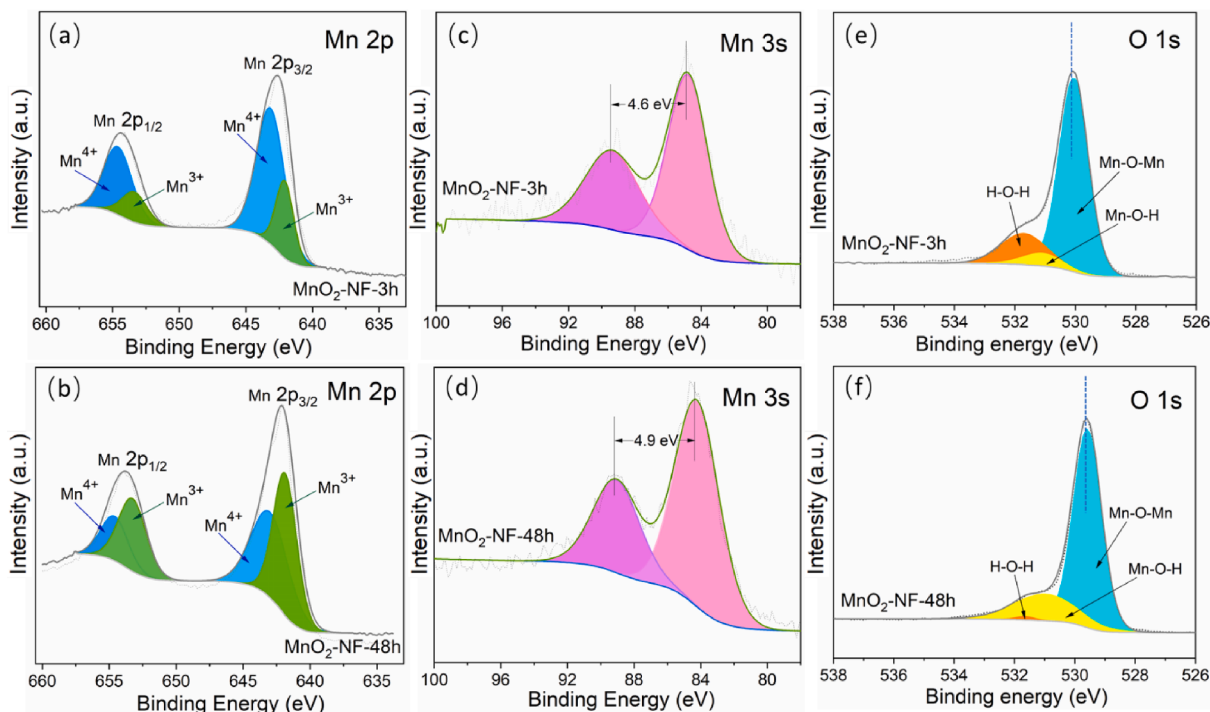


Fig. 3. Mn 2p XPS spectra of (a) MnO₂-NF-3h and (b) MnO₂-NF-48h; Mn 3s XPS spectra of (c) MnO₂-NF-3h and (d) MnO₂-NF-48h; O 1s XPS spectra of (e) MnO₂-NF-3h and (f) MnO₂-NF-48h.

531.7 eV attributed to the -OH in adsorbed water molecules (H-O-H) [39,40]. As shown in Fig. 3e and f, the O_V/O_L ratio of MnO₂-NF-48h (0.30) is much higher than that of the MnO₂-NF-3h (0.09), suggesting that MnO₂-NF-48h sample contains more oxygen vacancies via the hydrothermal treatment, which would benefit the catalytic activities [41].

To further confirm the presence of different content of oxygen vacancies in the samples, the electron paramagnetic resonance spectroscopy (EPR) measurements were carried out. The semi-quantitative EPR analysis was conducted by the doubly integration of the signal area

obtained from the EPR spectra. As shown in Fig. 4, the symmetrical EPR signal peak at $g = 2.004$ was detected in both 3 h and 48 h samples, owing to unpaired electrons at the oxygen vacancy sites of active materials [42,43]. Meanwhile, the signal intensity could indicate the concentration of oxygen vacancies. The strong signal peak of MnO₂-NF-48h suggests spin density (oxygen vacancy amount) in sample MnO₂-NF-48h much higher than that in sample MnO₂-NF-3h [42]. In addition, consistent with the previous report that Mn³⁺ defect site exists next to oxygen vacancy, the XPS and EPR results suggest that the MnO₂-NF-48h

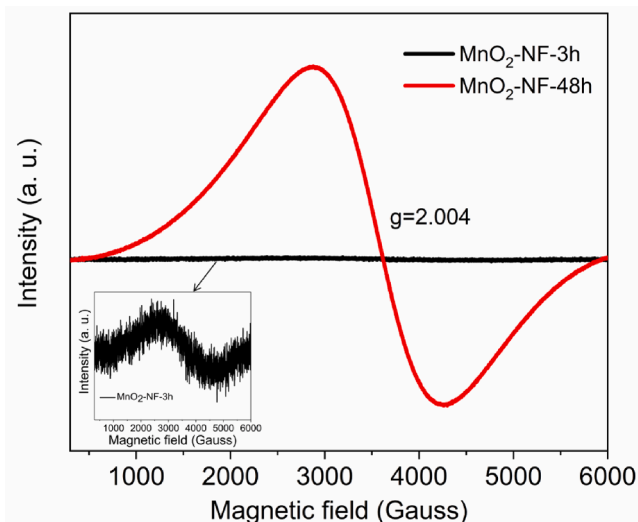


Fig. 4. EPR spectra of MnO₂-NF-3h and MnO₂-NF-48h (the insert image is the EPR spectra of MnO₂-NF-3h).

sample with abundant Mn³⁺ defects and oxygen vacancies would facilitate better catalytic performance [16].

The phase evolution process of MnO₂ through different reaction times is illustrated in Fig. 5. It is well known that the concentration of alkali metal cations has an influence on the phase formation of MnO₂ [34]. Firstly, as shown in Fig. S6, the solution for synthesizing MnO₂ was still purple, the same colour as KMnO₄ solution after 3 h reaction. It implies that the KMnO₄ was not fully involved during the 3 h reaction, suggesting that excessive K⁺ existed in the solution and a certain amount of K⁺ ions and water molecules were inserted into the interlayer space of δ-MnO₂. These are also confirmed by the XRD and TEM-EDS (Fig. S5a) patterns. The nanosheets together with K⁺ formed the layered δ-MnO₂ structures, which were held together by electrostatic forces [34]. The electrostatic forces between δ-MnO₂ layers were decreased with the increased reaction time, and the MnO₆ octahedra transformed to a disorder arrangement from the high crystallinity of δ-MnO₂, which could be concluded from the XRD pattern in Fig. S2c and d. With the increased reaction time, continuous energy and pressure caused the layered structure to collapse [44,45]. Secondly, since the K⁺ ions were constantly inserted into the layers built by MnO₆ octahedra, the

concentration of K⁺ in this work was not enough to support the layered structure of δ-MnO₂. Subsequently, the peaks of MnO₂-NF-24h are weaker; and some peaks are considered as the poor crystallinity of δ-MnO₂ [46,47]. With the time increasing, α-MnO₂ with 2 × 2 tunnels were formed. Since the moderate K⁺ ions with suitable radius are readily inserted into the 2 × 2 tunnels and continuously help to construct the stable structure (Fig. S5b), [34] the disordered MnO₆ octahedra were finally formed into 2 × 2 tunnels α-MnO₂ with the reaction time increasing. For the entire reaction process, layered-type δ-MnO₂ exists as an intermediate state in our system and then transformed to α phase with 2 × 2 tunnels structure [44,45].

On the one hand, the surface morphology evolution could boost the surface area of MnO₂, leading to more exposure of active sites for improving catalysis ability. On the other hand, the MnO₂-NF-48h sample contains much more oxygen vacancies and Mn³⁺ defects than MnO₂-NF-3h, which were expected to benefit electrocatalytic properties [16]. Hence, the synthesized MnO₂ with unique microstructure, rich oxygen vacancies, and Mn³⁺ sites are expected to dramatically alter its electronic and electrocatalytic properties for water splitting, as confirmed by experiments below.

3.2. Electrochemical performance

The catalytic performance of MnO₂-NF with three representative reaction times at 3, 24, and 48 h was investigated by polarization curves in alkaline KOH electrolytes. As a comparison, the OER and HER activities of pure NF were also included under the same test conditions.

As shown in Fig. 6a, all MnO₂-NF samples show better OER performance than that of NF, and α phase sample (MnO₂-NF-48h) exhibits better OER activity than δ phase sample (MnO₂-NF-3h) (the first peak around 1.4 V (vs RHE) for the NF is assigned to the oxidation of Ni²⁺/Ni³⁺ mediated by OH⁻ [48]). MnO₂-NF-48h exhibits the best electrocatalytic activity for OER with an overpotential (η) of 0.45 V at 50 mA cm⁻², much lower than that of MnO₂-NF-3h (0.53 V) and NF (0.55 V). Moreover, the Tafel slope (Fig. 6b) of MnO₂-NF-48h is 123 mV dec⁻¹, which was smaller than that of MnO₂-NF-3h (131 mV dec⁻¹) and MnO₂-NF-24h (147 mV dec⁻¹), suggesting a faster reaction kinetic.

Compared to OER, MnO₂ has been rarely studied in relation to HER [49–52]. There is great interest in the discovery of low-cost bifunctional electrocatalysts with excellent activity for overall water splitting. For HER activities in our project, as revealed in Fig. 6c, MnO₂-NF shows significantly enhanced performance compared to pristine NF, and the α

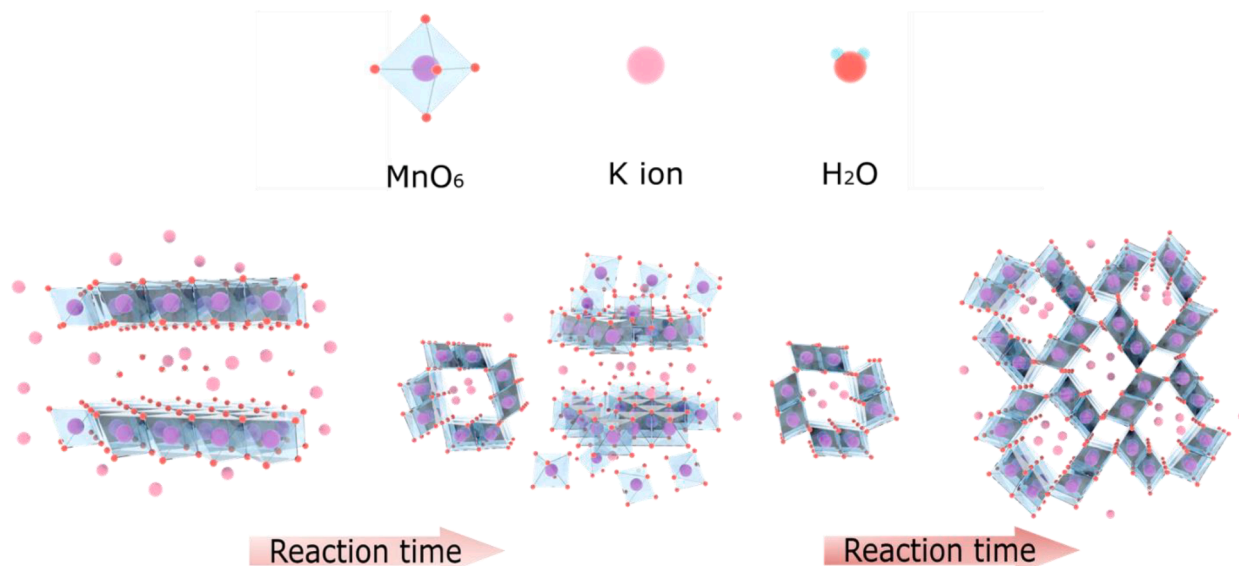


Fig. 5. Schematic diagram of the phase transition process of MnO₂-NF.

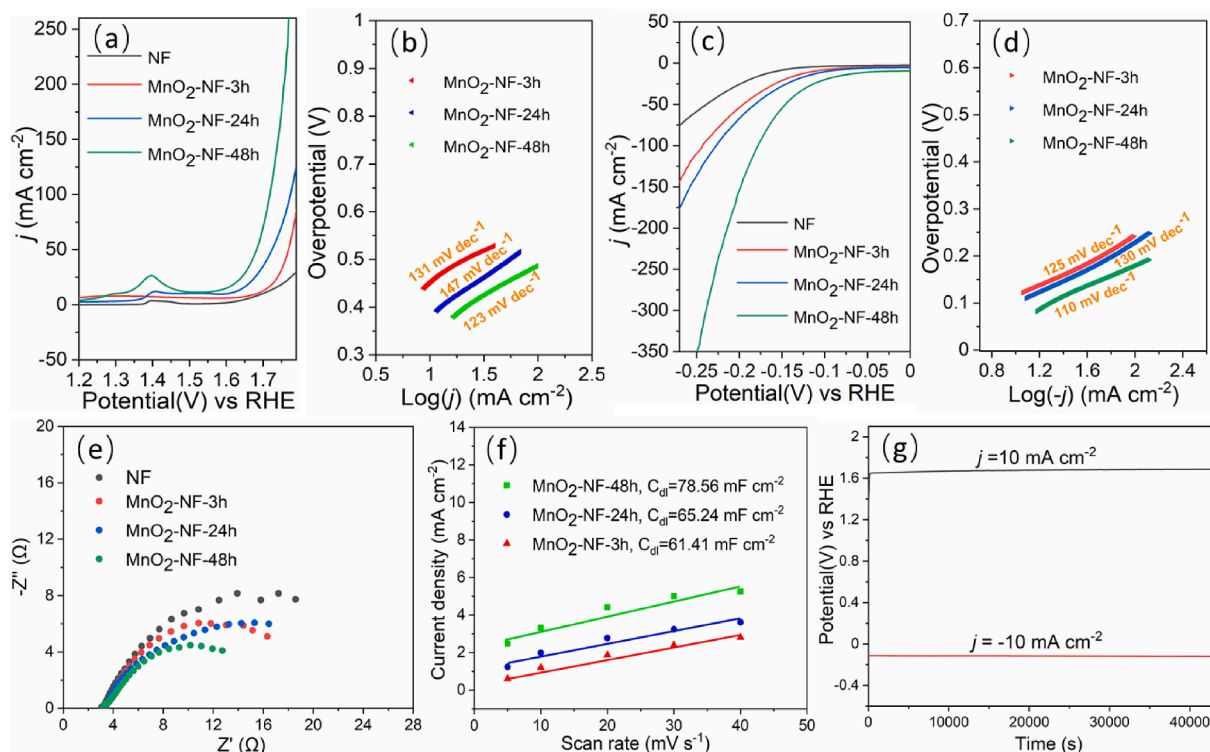


Fig. 6. (a) OER LSV curves of NF, MnO₂-NF-3h, MnO₂-NF-24h and MnO₂-NF-48h; (b) Corresponding Tafel slopes; (c) HER LSV curves of NF, MnO₂-NF-3h, MnO₂-NF-24h and MnO₂-NF-48h; (d) Corresponding Tafel slopes; (e) Nyquist plots of NF, MnO₂-NF-3h, MnO₂-NF-24h and MnO₂-NF-48h at 1.65 V (vs RHE) without iR compensation; (f) Determination of C_{dl} from the CV test for ECSA; (g) Chronopotentiometric curve of MnO₂-NF-48h for OER and HER at 10 mA cm⁻².

phase sample (MnO₂-NF-48h) exhibits better HER performance. At the same current density of 50 mA cm⁻², the overpotentials for H₂ evolution were 0.14 V for MnO₂-NF-48h (which are much lower than other reports [16,53]), 0.18 V for MnO₂-NF-24h, 0.19 V for MnO₂-NF-3h, and 0.23 V for NF. MnO₂-NF-48h sample exhibits superior performance at high current densities, which can achieve the current density of 150 mA cm⁻² at the overpotential of 0.198 V compared to 0.273 V for the MnO₂-NF-3h electrode. Tafel plots were constructed (Fig. 6d), with slopes increasing in the order of MnO₂-NF-48h (110 mV dec⁻¹) < MnO₂-NF-3h (125 mV dec⁻¹) < MnO₂-NF-24h (130 mV dec⁻¹). The above results suggest that the MnO₂-NF-48h sample is also a promising HER electrocatalyst.

To better understand the mechanism of the enhanced overall water splitting performance of MnO₂-NF, charge transfer properties are investigated by the EIS at 1.65 V (vs RHE). As shown in Fig. 6e, the EIS spectra reveal that the electrical conductivity of the α phase MnO₂-NF-48h significantly increases; and the dramatically reduced resistance would facilitate electron transfer and thereby benefit OER and HER performance. [24] The enhancement of conductivity could be attributed to the abundant Mn³⁺ active sites, which give α -MnO₂-NF high electrical conductivity and improved reaction kinetics [9,16]. The high conductivity of NF benefits charge transfer and electrical contact as well. Furthermore, the ECSA of MnO₂-NF and NF electrodes was first estimated using the C_{dl} . As displayed in Fig. 6f and S7, the C_{dl} value of α phase MnO₂-NF-48h was measured to be 78.56 mF cm⁻², which is higher than those of the δ phase MnO₂-NF-3h (61.41 mF cm⁻²). The enlarged ECSA improved the catalytic activity of α -MnO₂-NF with more exposed catalytic sites. It should be noted that nanowire structures can significantly boost the surface area and retain high conductivity for charge transfer during the catalysis process [20]. Therefore, the MnO₂ with fine crystal structure and optimized surface morphology for high-performing electrochemical catalysis was successfully introduced in this work. Durability is also a critical factor for practical applications. The long-term cycling performance of α -MnO₂-NF was measured at the current density of 10 mA cm⁻² and 100 mA cm⁻² for OER and HER,

respectively. As shown in Fig. 6g and S8, there is no noticeable decrease in the current density after testing for 12 h in 1 M KOH, suggesting the satisfied long-term stability under this condition. In addition, as shown in Fig S9 and 10, both XRD and SEM results of post-OER and post-HER MnO₂-NF-48h were demonstrated. It can be found that both crystal structures and morphologies were maintained. The maintained nanowires-nanosheets morphology of the α -MnO₂ indicates the excellent stability of the electrode. (Comparison with catalytic performances of selected previously reported MnO₂ electrocatalysts were listed in Table S1. In addition, a comparison of catalytic performance between different phases of MnO₂ nanopowder (Fig. S3a, S11 and S12) and in-situ growth MnO₂ were provided in supporting information.)

3.3. DFT studies of α -MnO₂ and δ -MnO₂

The above structural characterization and electrochemical test indicated that the improved electrochemical activity could be attributed to the abundant oxygen vacancies and unsaturated Mn³⁺ active sites formed on the surface of α -MnO₂-NF [16]. To further understand how the electronic band properties of the α -MnO₂ and δ -MnO₂ polymorphs affect their electrocatalytic performances, first-principles calculations based on density functional theory (DFT) were performed (Fig. 7). Our DFT results show that the band gap, E_g , of the δ polymorph is about 1.0 eV larger than that of the α polymorph, both for stoichiometric and non-stoichiometric (i.e., oxygen deficient) compositions. Metal oxides with small band gaps exhibit better electronic conductivity, thus suggesting improved electronic transfer and electrocatalytic activities [54,55]. In particular, we estimated $E_g = 1.8$ eV for α -MnO₂ and 2.7 eV for δ -MnO₂ (Fig. 7a and b), and only relatively small E_g variations appeared upon the generation of oxygen vacancies (besides the emergence of sparse mid-gap states concentrated in one of the two spin channels, Fig. 7c and d). We also estimated the alignment of the MnO₂ valence and conduction bands (VB and CB, respectively) as referred to the vacuum level (E_V) (see Supporting Information for the technical details of this type of

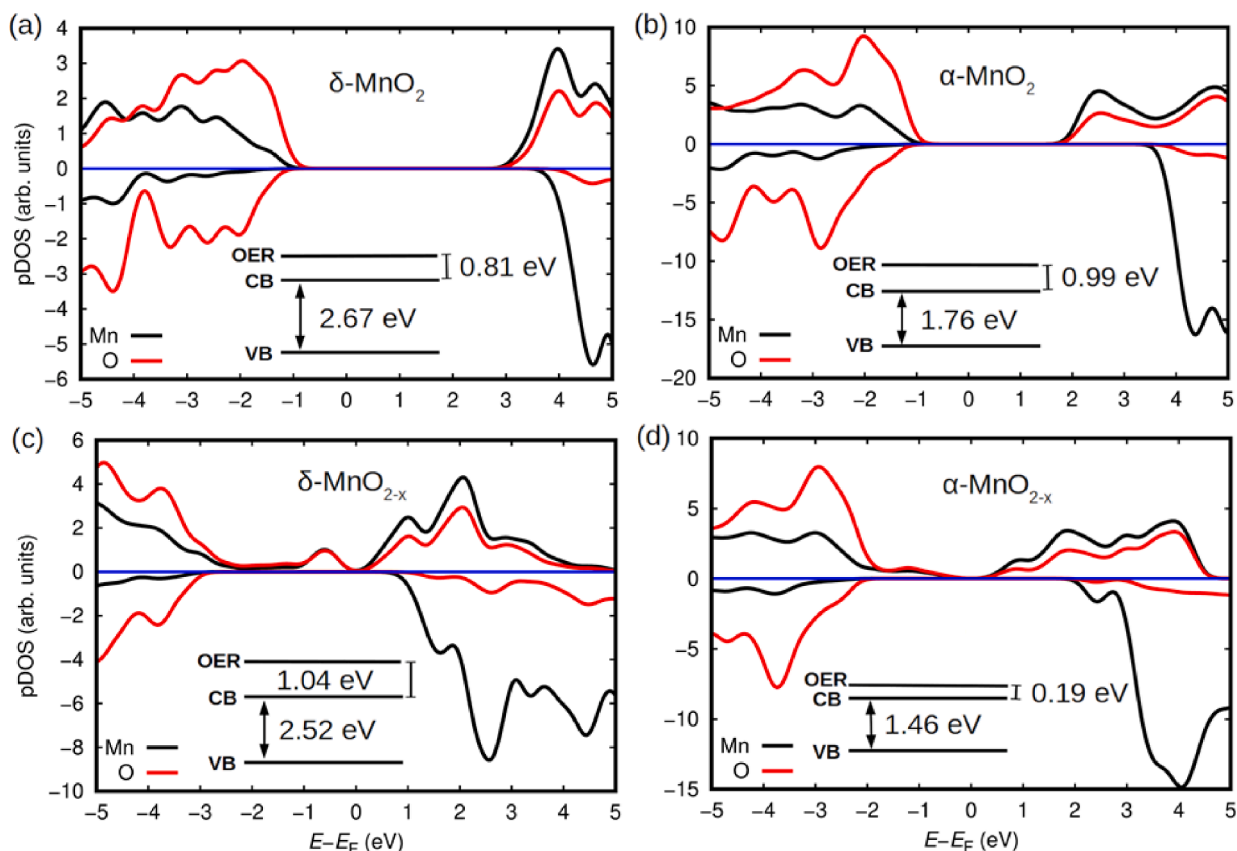


Fig. 7. Theoretical estimation of the electronic band structure properties of (a) δ - and (b) α - MnO_2 and of (c) δ - and (d) α - MnO_{2-x} based on first-principles DFT calculations. Spin-up (spin-down) electronic density of states are represented with positive (negative) values. “OER” stands for the energy level of the oxygen evolution reaction ($\text{O}_2/\text{H}_2\text{O}$), “CB” for the alignment of the conduction band, and “VB” for the alignment of the valence band.

calculations). For stoichiometric MnO_2 , it was found that the energy level differences $\Delta E_{\text{VB}} = E_{\text{V}} - E_{\text{VB}}$ and $\Delta E_{\text{CB}} = E_{\text{V}} - E_{\text{CB}}$ amount to 6.62 eV and 8.39 eV for α - MnO_2 and to 6.44 eV and 9.11 eV for δ - MnO_2 , respectively (Fig. 7a and b). It is noted that due to the neglect of electrolyte-induced effects and the presence of K^+ ions, our estimated band alignments are likely to be significantly shifted with respect to those of the real samples analyzed in the experiments. Importantly, upon the generation of oxygen vacancies, it was found that only the energy levels of the α - MnO_2 polymorph changed appreciably. Specifically, for α - MnO_{2-x} the energy differences ΔE_{VB} and ΔE_{CB} amount to 5.82 eV and 7.28 eV and for δ - MnO_{2-x} to 6.67 eV and 9.18 eV (Fig. 7c and d). We tentatively ascribe the origin of the poor band gap tunability estimated for δ - MnO_2 to its stacking layer structure.

Therefore, based on our theoretical DFT calculations (as shown in Fig. S13), it can be concluded that the α - MnO_{2-x} polymorph is expected to exhibit better electrocatalytic performance than δ - MnO_2 due to: (1) a more suitable energy band gap (which leads to improved electronic conductivity and transfers), and (2) superior band alignment tunability through the creation of oxygen vacancies (which allows for efficient improvement of the electrocatalytic performance via chemical synthesis routes).

4. Conclusion

In summary, MnO_2 nanostructures on nickel foam with controlled phases have been prepared by simply tuning the reaction time and were further utilized as efficient binder-free overall electrocatalysts for water splitting. The structure transition of MnO_2 was attributed to the reaction time and free K^+ in the solution, and δ - MnO_2 played as an intermediate state in the system that generates the α - MnO_2 . The enhanced overall

water-splitting performance of MnO_2 -NF-48h (α phase) was due to the following factors: (i) the morphology of nanowires and nanosheets enlarged the specific surface area of MnO_2 , which exposed more catalytic active sites, (ii) abundant oxygen vacancies and Mn ion defects generated from the hydrothermal treatment exist as active sites, (iii) excellent reaction kinetics for both OER and HER, (iv) more suitable bandgap (~ 1.0 eV smaller than the δ polymorph) and fine-tuned band alignment. This work could provide a guideline to tailor the properties of target MnO_2 and might be of great potential to synthesize other metal-oxides-based electrocatalysts.

Declaration of Competing Interest

The authors declare that they have no known competing financial interests or personal relationships that could have appeared to influence the work reported in this paper.

Acknowledgments

This research was partially supported by funding from the UNSW Digital Grid Futures Institute, UNSW, Sydney, under a cross disciplinary fund scheme. D. Chu acknowledges the financial support from the Australian Research Council.

Appendix A. Supplementary data

Supplementary data to this article can be found online at <https://doi.org/10.1016/j.cej.2022.135561>.

References

- [1] J. Wang, Y. Gao, H. Kong, J. Kim, S. Choi, F. Ciucci, Y. Hao, S. Yang, Z. Shao, J. Lim, Non-precious-metal catalysts for alkaline water electrolysis: operando characterizations, theoretical calculations, and recent advances, *Chem. Soc. Rev.* 49 (24) (2020) 9154–9196, <https://doi.org/10.1039/D0CS00575D>.
- [2] L. Zhang, H. Zhao, S. Xu, Q. Liu, T. Li, Y. Luo, S. Gao, X. Shi, A.M. Asiri, X. Sun, Recent Advances in 1D Electrospun Nanocatalysts for Electrochemical Water Splitting, *Small Structures* 2 (2021) 2000048, <https://doi.org/10.1002/sstr.202000048>.
- [3] M. Li, K. Duanmu, C. Wan, T. Cheng, L. Zhang, S. Dai, W. Chen, Z. Zhao, P. Li, H. Fei, Y. Zhu, R. Yu, J. Luo, K. Zang, Z. Lin, M. Ding, J. Huang, H. Sun, J. Guo, X. Pan, W.A. Goddard, P. Sautet, Y.u. Huang, X. Duan, Single-atom tailoring of platinum nanocatalysts for high-performance multifunctional electrocatalysis, *Nat. Catal.* 2 (6) (2019) 495–503, <https://doi.org/10.1038/s41929-019-0279-6>.
- [4] J. Mahmood, F. Li, S.-M. Jung, M.S. Okay, I. Ahmad, S.-J. Kim, N. Park, H. Y. Jeong, J.-B. Baek, An efficient and pH-universal ruthenium-based catalyst for the hydrogen evolution reaction, *Nat. Nanotechnol.* 12 (5) (2017) 441–446, <https://doi.org/10.1038/nnano.2016.304>.
- [5] F. Li, G.-F. Han, H.-J. Noh, J.-P. Jeon, I. Ahmad, S. Chen, C. Yang, Y. Bu, Z. Fu, Y. Lu, J.-B. Baek, Balancing hydrogen adsorption/desorption by orbital modulation for efficient hydrogen evolution catalysis, *Nat. Commun.* 10 (2019) 4060, <https://doi.org/10.1038/s41467-019-12012-z>.
- [6] Z. Su, T. Chen, Porous Noble Metal Electrocatalysts: Synthesis, Performance, and Development, *Small : nano micro.* 17 (2021) 2005354, <https://doi.org/10.1002/sml.202005354>.
- [7] Q. Shi, C. Zhu, D. Du, Y. Lin, Robust noble metal-based electrocatalysts for oxygen evolution reaction, *Chem. Soc. Rev.* 48 (12) (2019) 3181–3192, <https://doi.org/10.1039/C8CS00671G>.
- [8] Y. Wang, B. Liu, X. Shen, H. Arandiyani, T. Zhao, Y. Li, M. Garbrecht, Z. Su, L. Han, A. Tricoli, C. Zhao, Engineering the Activity and Stability of MOF-Nanocomposites for Efficient Water Oxidation, *Adv. Energy Mater.* 11 (2021) 2003759, <https://doi.org/10.1002/aenm.202003759>.
- [9] J. Lu, H. Wang, Y. Sun, X. Wang, X. Song, R. Wang, Charge state manipulation induced through cation intercalation into MnO₂ sheet arrays for efficient water splitting, *Chem. Eng. J.* 417 (2021), 127894, <https://doi.org/10.1016/j.cej.2020.127894>.
- [10] C. Ye, L. Zhang, L. Yue, B. Deng, Y. Cao, Q. Liu, Y. Luo, S. Lu, B. Zheng, X. Sun, A NiCo LDH nanosheet array on graphite felt: an efficient 3D electrocatalyst for the oxygen evolution reaction in alkaline media, *Inorg. Chem. Front.* 8 (12) (2021) 3162–3166, <https://doi.org/10.1039/D1QI00428J>.
- [11] C. Meng, Y. Cao, Y. Luo, F. Zhang, Q. Kong, A.A. Alshehri, K.A. Alzahrani, T. Li, Q. Liu, X. Sun, A Ni-MOF nanosheet array for efficient oxygen evolution electrocatalysis in alkaline media, *Inorg. Chem. Front.* 8 (12) (2021) 3007–3011, <https://doi.org/10.1039/D1QI00345C>.
- [12] S. Xu, Y. Du, X. Yu, Z. Wang, X. Cheng, Q. Liu, Y. Luo, X. Sun, Q.i. Wu, A Cr-FeOOH@Ni-P/NF binder-free electrode as an excellent oxygen evolution reaction electrocatalyst, *Nanoscale* 13 (40) (2021) 17003–17010, <https://doi.org/10.1039/D1NR04513J>.
- [13] P. Ding, C. Meng, J. Liang, T. Li, Y. Wang, Q. Liu, Y. Luo, G. Cui, A.M. Asiri, S. Lu, X. Sun, NiFe Layered-Double-Hydroxide Nanosheet Arrays on Graphite Felt: A 3D Electrocatalyst for Highly Efficient Water Oxidation in Alkaline Media, *Inorg. Chem.* 60 (17) (2021) 12703–12708, <https://doi.org/10.1021/acs.inorgchem.1c01783>.
- [14] X. Yu, S. Xu, Z. Wang, S. Wang, J. Zhang, Q. Liu, Y. Luo, Y. Du, X. Sun, Q.i. Wu, Self-supported Ni₃S₂@Ni₂P/MoS₂ heterostructures on nickel foam for an outstanding oxygen evolution reaction and efficient overall water splitting, *Dalton Trans.* 50 (42) (2021) 15094–15102, <https://doi.org/10.1039/D1DT03023J>.
- [15] H. Antoni, D.M. Morales, J. Bitzer, Q. Fu, Y.-T. Chen, J. Masa, W. Kleist, W. Schuhmann, M. Muhler, Enhancing the water splitting performance of cryptomelane-type α-(K)MnO₂, *J. Catal.* 374 (2019) 335–344, <https://doi.org/10.1016/j.jcat.2019.05.010>.
- [16] Y. Zhao, C. Chang, F. Teng, Y. Zhao, G. Chen, R. Shi, G.I.N. Waterhouse, W. Huang, T. Zhang, Defect-Engineered Ultrathin δ-MnO₂ Nanosheet Arrays as Bifunctional Electrodes for Efficient Overall Water Splitting, *Adv. Energy Mater.* 7 (18) (2017) 1700005, <https://doi.org/10.1002/aenm.201700005>.
- [17] S. Ni, H. Zhang, Y. Zhao, X. Li, Y. Sun, J. Qian, Q. Xu, P. Gao, D. Wu, K. Kato, M. Yamauchi, Y. Sun, Single atomic Ag enhances the bifunctional activity and cycling stability of MnO₂, *Chem. Eng. J.* 366 (2019) 631–638, <https://doi.org/10.1016/j.cej.2019.02.084>.
- [18] J.H. Hong, J.H. Kim, G.D. Park, J.Y. Lee, J.-K. Lee, Y.C. Kang, A strategy for fabricating three-dimensional porous architecture comprising metal oxides/CNT as highly active and durable bifunctional oxygen electrocatalysts and their application in rechargeable Zn-air batteries, *Chem. Eng. J.* 414 (2021), 128815, <https://doi.org/10.1016/j.cej.2021.128815>.
- [19] Y. Meng, W. Song, H. Huang, Z. Ren, S.-Y. Chen, S.L. Suib, Structure-Property Relationship of Bifunctional MnO₂ Nanostructures: Highly Efficient, Ultra-Stable Electrochemical Water Oxidation and Oxygen Reduction Reaction Catalysts Identified in Alkaline Media, *J. Am. Chem. Soc.* 136 (32) (2014) 11452–11464, <https://doi.org/10.1021/ja505186m>.
- [20] G. Yan, Y. Lian, Y. Gu, C. Yang, H. Sun, Q. Mu, Q. Li, W. Zhu, X. Zheng, M. Chen, J. Zhu, Z. Deng, Y. Peng, Phase and Morphology Transformation of MnO₂ Induced by Ionic Liquids toward Efficient Water Oxidation, *ACS Catal.* 8 (11) (2018) 10137–10147, <https://doi.org/10.1021/acscatal.8b02203>.
- [21] Y. Gu, G. Yan, Y. Lian, P. Qi, Q. Mu, C. Zhang, Z. Deng, Y. Peng, MnIII-enriched α-MnO₂ nanowires as efficient bifunctional oxygen catalysts for rechargeable Zn-air batteries, *Energy Stor. Mater.* 23 (2019) 252–260, <https://doi.org/10.1016/j.ensm.2019.05.006>.
- [22] A. Grimaud, W.T. Hong, Y. Shao-Horn, J.-M. Tarascon, Anionic redox processes for electrochemical devices, *Nat. Mater.* 15 (2) (2016) 121–126, <https://doi.org/10.1038/nmat4551>.
- [23] Y. Chen, D.D. Fong, F.W. Herbert, J. Rault, J.-P. Rueff, N. Tsvetkov, B. Yildiz, Modified Oxygen Defect Chemistry at Transition Metal Oxide Heterostructures Probed by Hard X-ray Photoelectron Spectroscopy and X-ray Diffraction, *Chem. Mater.* 30 (10) (2018) 3359–3371, <https://doi.org/10.1021/acs.chemmater.8b00808>.
- [24] M. Li, B. Cai, R. Tian, X. Yu, M.B.H. Breese, X. Chu, Z. Han, S. Li, R. Joshi, A. Vinu, T. Wan, Z. Ao, J. Yi, D. Chu, Vanadium doped 1T MoS₂ nanosheets for highly efficient electrocatalytic hydrogen evolution in both acidic and alkaline solutions, *Chem. Eng. J.* 409 (2021), 128158, <https://doi.org/10.1016/j.cej.2020.128158>.
- [25] Y. Zhou, F. Chen, R. Tian, S. Huang, R. Chen, M. Li, T. Wan, Z. Han, D. Wang, D. Chu, Oxygen vacancies and band gap engineering of vertically aligned MnO₂ porous nanosheets for efficient oxygen evolution reaction, *Surf. Interfaces.* 26 (2021), 101398, <https://doi.org/10.1016/j.surfin.2021.101398>.
- [26] C. Cazorla, J. Boronat, Simulation and understanding of atomic and molecular quantum crystals, *Rev. Mod. Phys.* 89 (2017), 035003, <https://doi.org/10.1103/RevModPhys.89.035003>.
- [27] J.P. Perdew, A. Ruzsinszky, G.I. Csonka, O.A. Vydrov, G.E. Scuseria, L. A. Constantin, X. Zhou, K. Burke, Restoring the Density-Gradient Expansion for Exchange in Solids and Surfaces, *Phys. Rev. Lett.* 100 (2008), 136406, <https://doi.org/10.1103/PhysRevLett.100.136406>.
- [28] G. Kresse, J. Furthmüller, Efficient iterative schemes for ab initio total-energy calculations using a plane-wave basis set, *Phys. Rev. B* 54 (16) (1996) 11169–11186, <https://doi.org/10.1103/PhysRevB.54.11169>.
- [29] S.L. Dudarev, G.A. Botton, S.Y. Savrasov, C.J. Humphreys, A.P. Sutton, Electron-loss spectra and the structural stability of nickel oxide: An LSDA+U study, *Phys. Rev. B* 57 (1998) 1505–1509, <https://doi.org/10.1103/PhysRevB.57.1505>.
- [30] P.E. Blöchl, Projector augmented-wave method, *Phys. Rev. B* 50 (24) (1994) 17953–17979, <https://doi.org/10.1103/PhysRevB.50.17953>.
- [31] E.N. Brothers, A.F. Izmaylov, J.O. Normand, V. Barone, G.E. Scuseria, Accurate solid-state band gaps via screened hybrid electronic structure calculations, *J. Chem. Phys.* 129 (1) (2008) 011102, <https://doi.org/10.1063/1.2955460>.
- [32] Z. Liu, C. Menéndez, J. Shenoy, J.N. Hart, C.C. Sorrell, C. Cazorla, Strain engineering of oxide thin films for photocatalytic applications, *Nano Energy* 72 (2020), 104732, <https://doi.org/10.1016/j.nanoen.2020.104732>.
- [33] C. Julien, M. Massot, S. Rangan, M. Lemal, D. Guyomard, Study of structural defects in γ-MnO₂ by Raman spectroscopy, *J. Raman Spectrosc.* 33 (2002) 223–228.
- [34] B. Yin, S. Zhang, H.e. Jiang, F. Qu, X. Wu, Phase-controlled synthesis of polymorphic MnO₂ structures for electrochemical energy storage, *J. Mater. Chem. A* 3 (10) (2015) 5722–5729, <https://doi.org/10.1039/C4TA06943A>.
- [35] Y. Yuan, W. Yao, B.W. Byles, E. Pomerantseva, K. Amine, R. Shahbazian-Yassar, J. Lu, Revealing the Atomic Structures of Exposed Lateral Surfaces for Polymorphic Manganese Dioxide Nanowires, *Small Structures* 2 (2021) 2000091, <https://doi.org/10.1002/sstr.202000091>.
- [36] J. Jia, P. Zhang, L. Chen, The effect of morphology of α-MnO₂ on catalytic decomposition of gaseous ozone, *Catal. Sci. Technol.* 6 (15) (2016) 5841–5847, <https://doi.org/10.1039/C6CY00301J>.
- [37] K. Li, C. Chen, H. Zhang, X. Hu, T. Sun, J. Jia, Effects of phase structure of MnO₂ and morphology of δ-MnO₂ on toluene catalytic oxidation, *Appl. Surf. Sci.* 496 (2019), 143662, <https://doi.org/10.1016/j.apsusc.2019.143662>.
- [38] S. Liang, F. Teng, G. Bulgan, R. Zong, Y. Zhu, Effect of Phase Structure of MnO₂ Nanorod Catalyst on the Activity for CO Oxidation, *J. Phys. Chem. C* 112 (14) (2008) 5307–5315, <https://doi.org/10.1021/jp0774995>.
- [39] J. Yin, Y. Li, F. Lv, M. Lu, K. Sun, W. Wang, L. Wang, F. Cheng, Y. Li, P. Xi, S. Guo, Oxygen Vacancies Dominated NiS₂/CoS₂ Interface Porous Nanowires for Portable Zn-Air Batteries Driven Water Splitting Devices, *Adv. Mater.* 29 (2017) 1704681, <https://doi.org/10.1002/adma.201704681>.
- [40] Y. Zhang, J. Fu, H. Zhao, R. Jiang, F. Tian, R. Zhang, Tremella-like Ni₃S₂/MnS with ultrathin nanosheets and abundant oxygen vacancies directly used for high speed overall water splitting, *Appl. Catal. B-Environ.* 257 (2019), 117899, <https://doi.org/10.1016/j.apcatb.2019.117899>.
- [41] Y. Hou, J. Wang, C. Hou, Y. Fan, Y. Zhai, H. Li, F. Dang, S. Chou, Oxygen vacancies promoting the electrocatalytic performance of CeO₂ nanorods as cathode materials for Li-O₂ batteries, *J. Mater. Chem. A* 7 (11) (2019) 6552–6561, <https://doi.org/10.1039/C9TA00882A>.
- [42] S. Mo, Q. Zhang, J. Li, Y. Sun, Q. Ren, S. Zou, Q. Zhang, J. Lu, M. Fu, D. Mo, J. Wu, H. Huang, D. Ye, Highly efficient mesoporous MnO₂ catalysts for the total toluene oxidation: Oxygen-Vacancy defect engineering and involved intermediates using in situ DRIFTS, *Appl. Catal. B* 264 (2020), 118464, <https://doi.org/10.1016/j.apcatb.2019.118464>.
- [43] Y.-C. Zhang, Z. Li, L. Zhang, L. Pan, X. Zhang, L. Wang, A. Fazal, E. J.-J. Zou, Role of oxygen vacancies in photocatalytic water oxidation on ceria oxide: Experiment and DFT studies, *Appl. Catal. B* 224 (2018) 101–108, <https://doi.org/https://doi.org/10.1016/j.apcatb.2017.10.049>.
- [44] X. Wang, Y. Li, Synthesis and Formation Mechanism of Manganese Dioxide Nanowires/Nanorods, *Chem. Eur. J.* 9 (2003) 300–306, <https://doi.org/10.1002/chem.200390024>.
- [45] S. Rong, P. Zhang, F. Liu, Y. Yang, Engineering Crystal Facet of α-MnO₂ Nanowire for Highly Efficient Catalytic Oxidation of Carcinogenic Airborne Formaldehyde, *ACS Catal.* 8 (4) (2018) 3435–3446, <https://doi.org/10.1021/acscatal.8b00045>.

- [46] A. Valipour, N. Hamnabard, S.M.H. Meshkati, M. Pakan, Y.-H. Ahn, Effectiveness of phase- and morphology-controlled MnO₂ nanomaterials derived from flower-like δ-MnO₂ as alternative cathode catalyst in microbial fuel cells, *Dalton Trans.* 48 (16) (2019) 5429–5443, <https://doi.org/10.1039/C9DT00520J>.
- [47] Y. Xie, Y. Yu, X. Gong, Y. Guo, Y. Guo, Y. Wang, G. Lu, Effect of the crystal plane figure on the catalytic performance of MnO₂ for the total oxidation of propane, *CrystEngComm* 17 (15) (2015) 3005–3014, <https://doi.org/10.1039/C5CE00058K>.
- [48] Y. Gu, Z. Lu, Z. Chang, J. Liu, X. Lei, Y. Li, X. Sun, NiTi layered double hydroxide thin films for advanced pseudocapacitor electrodes, *J. Mater. Chem. A* 1 (2013) 10655–10661, <https://doi.org/10.1039/C3TA10954B>.
- [49] Y.-F. Li, Z.-P. Liu, Active Site Revealed for Water Oxidation on Electrochemically Induced δ-MnO₂: Role of Spinel-to-Layer Phase Transition, *J. Am. Chem. Soc.* 140 (5) (2018) 1783–1792, <https://doi.org/10.1021/jacs.7b11393>.
- [50] G. Elmaci, S. Cerci, D. Sunar-Cerci, The evaluation of the long-term stability of α-MnO₂ based OER electrocatalyst in neutral medium by using data processing approach, *J. Mol. Struct.* 1195 (2019) 632–640, <https://doi.org/10.1016/j.molstruc.2019.06.016>.
- [51] P.K. Gupta, A. Bhandari, S. Saha, J. Bhattacharya, R.G.S. Pala, Modulating Oxygen Evolution Reactivity in MnO₂ through Polymorphic Engineering, *J. Phys. Chem. C* 123 (36) (2019) 22345–22357, <https://doi.org/10.1021/acs.jpcc.9b05823>.
- [52] K. Fujimoto, T. Okada, M. Nakayama, Enhanced Oxygen Evolution Reaction Activity of Co Ions Isolated in the Interlayer Space of Buserite MnO₂, *J. Phys. Chem. C* 122 (15) (2018) 8406–8413, <https://doi.org/10.1021/acs.jpcc.8b01238>.
- [53] S. Bolar, S. Shit, P. Samanta, N. Chandra Murmu, T. Kuila, The structure–activity correlation of bifunctional MnO₂ polymorphic and MoS₂-based heterostructures: a highly efficient, robust electrochemical water oxidation and reduction reaction catalyst in alkaline pH, *Sustain. Energy Fuels* 5 (4) (2021) 1148–1157, <https://doi.org/10.1039/D0SE01714K>.
- [54] J. Wang, J. Liu, B. Zhang, F. Cheng, Y. Ruan, X. Ji, K. Xu, C. Chen, L. Miao, J. Jiang, Stabilizing the oxygen vacancies and promoting water-oxidation kinetics in cobalt oxides by lower valence-state doping, *Nano Energy* 53 (2018) 144–151, <https://doi.org/10.1016/j.nanoen.2018.08.022>.
- [55] Y. Zhu, L. Zhang, B. Zhao, H. Chen, X. Liu, R. Zhao, X. Wang, J. Liu, Y. Chen, M. Liu, Improving the Activity for Oxygen Evolution Reaction by Tailoring Oxygen Defects in Double Perovskite Oxides, *Adv. Funct. Mater.* 29 (2019) 1901783, <https://doi.org/10.1002/adfm.201901783>.